



ELSEVIER

Contents lists available at SciVerse ScienceDirect

## Earth and Planetary Science Letters

journal homepage: [www.elsevier.com/locate/epsl](http://www.elsevier.com/locate/epsl)

# Dynamics of explosive paroxysms at open-vent andesitic systems: High-resolution mass distribution analyses of the 2006 Tungurahua fall deposit (Ecuador)

Julia Eychenne<sup>a,b,c,\*</sup>, Jean-Luc Le Pennec<sup>a,b,c</sup>, Patricio Ramón<sup>d</sup>, Hugo Yepes<sup>d</sup>

<sup>a</sup> Clermont Université, Université Blaise Pascal, Laboratoire Magmas et Volcans, BP 10448, F-63000 Clermont-Ferrand, France

<sup>b</sup> CNRS, UMR 6524, Laboratoire Magmas et Volcans, 5 rue Kessler, 63038 Clermont-Ferrand cedex, France

<sup>c</sup> IRD, R 163, Laboratoire Magmas et Volcans, 5 rue Kessler, 63038 Clermont-Ferrand cedex, France

<sup>d</sup> Instituto Geofísico, Escuela Politécnica Nacional, Ap. 17-01-2759, Quito, Ecuador

## ARTICLE INFO

## Article history:

Received 10 May 2012

Received in revised form

25 October 2012

Accepted 1 November 2012

Editor: B. Marty

Available online 11 December 2012

## Keywords:

Tungurahua volcano

magnitude

intensity

density distributions

mass componentry distribution

## ABSTRACT

Long-lasting andesitic eruptions sometimes include strong short-lived explosive events, which can pose significant hazards in populated regions. The origin and dynamics of such violent eruptions remain poorly known and may involve a combination of different factors. Tungurahua volcano, Ecuador, reawakens in 1999 and is an example of such an open-vent system that experienced a strong and deadly andesitic pyroclastic flow-forming event in August 2006. Inspection of the deposits suggested that the event could have been triggered by magma mixing (coexistence of both silicic pumices and andesitic scoria in the tephra), magma–water interaction (presence of xenolithic clasts) or deep andesitic magma reinjection (based on mineral chemistry). Here we investigate these options by performing a high-resolution mass budget analysis of the scoria fall deposit. This is achieved by analysing componentry compositions and their mass distribution pattern in the layer, which allow us to document and integrate exponential and power laws mass decay rates over wide areas. The results yield a total mass for the tephra layer of  $\sim 2 \times 10^{10}$  kg. The pumice mass fraction is far too small ( $< 0.4\%$ ) to account for the high explosivity of the 2006 event. Similarly, the xenoclastic mass fraction is unexpectedly small (0.2%) and suggests limited magma–water interaction. Instead, we interpret these xenoclasts as a result of upper conduit erosion at a rate of  $\sim 30$  cm/h during the paroxysm. Altogether our results support an explosive event fed by a deep gas-rich andesitic reinjection, which would have incorporated a pocket of older differentiated magma and eroded the upper conduit during the sub-plinian event. The high-resolution mass-based approach reveals useful to decipher the origin of the violent 2006 paroxysm and has potential to improve magnitude determinations of ancient eruption by considering componentry mass instead of volume. It is also applicable for monitoring purposes in the context of ongoing crises at andesitic volcanoes worldwide

© 2012 Elsevier B.V. All rights reserved.

## 1. Introduction

Many andesitic volcanoes at subduction plate margins can experience, in the course of their evolution, periods of sub-continuous eruption lasting years, decades, or centuries. These periods are characterised by outgassing events, extrusion of viscous lava flows and domes (e.g. Colima in Mexico (Saucedo et al., 2005; Varley et al., 2010), Merapi in Indonesia (Camus et al., 2000; Charbonnier and Gertisser, 2008; Gertisser and Keller, 2003), Arenal in Costa Rica (Cole et al., 2005; Szramek et al., 2006), and by explosive activity of uneven intensity (e.g. Sakurajima in Japan (Miwa et al., 2009; Yamanoi et al., 2008), Sangay in Ecuador (Monzier et al., 1999)). Such open-vent

eruptive periods may be punctuated by strong explosive events of short duration, with potential generation of pyroclastic flows on the volcano flanks and beyond. In populated areas these explosions are highly hazardous because they take place with little or no warning, and geochemical and geophysical precursors are commonly concealed in a background of complex seismic and degassing signals. Recent deadly and damaging examples at Arenal, Costa-Rica (e.g. 2000) (Alvarado and Soto, 2002; Szramek et al., 2006), Colima, Mexico (e.g. 2003) (Savov et al., 2008) and Merapi, Indonesia (e.g. 2010) (Gertisser et al., 2011) illustrate these situations. Understanding why and how these paroxysmal explosions occur remains a major challenge of volcanology, and this issue deserves enhanced research effort for the sake of volcanic hazard analyses and eruptive scenarios proposal.

The andesitic Tungurahua volcano, central Ecuador, has experienced open-vent activity since its reawakening in mid-1999, with successive eruptive phases of small to moderate size and intensity

\* Corresponding author at: Clermont Université, Université Blaise Pascal, Laboratoire Magmas et Volcans, BP 10448, F-63000 Clermont-Ferrand, France. Tel.: +33 4 73 34 67 23; fax: +33 4 73 34 67 44.

E-mail address: J.Eychenne@opgc.univ-bpclermont.fr (J. Eychenne).

(Le Pennec et al., 2012; Samaniego et al., 2011; Steffke et al., 2010; Wright et al., 2012). Seven years after the onset of the magmatic activity, a powerful pyroclastic flow-forming event occurred on August 16th, 2006, killing seven and severely impacting nearby urban and rural communities. A tephra column rose up to more than 15 km above the crater and deposited a scoria fall layer to the West. The origin and dynamics of this remarkably strong explosive event, in a context of sub-continuous activity, have remained unclear. After the eruption and several field inspections of the pyroclastic products in late August 2006, three options were considered to explain the exceptionally high explosivity of the August 16th event. The presence in the andesitic tephra fall deposit, for the very first time since 1999, of many (1) silicic whitish pumice clasts and (2) xenolithic particles, suggested the possible occurrence in the course of the open-vent andesitic eruption, of (1) a magma mixing event and/or (2) energetic magma–water interactions, as a cause of the violent explosion. Alternatively, Samaniego et al. (2011) investigated the petrology of the juvenile products and proposed that the eruption was possibly triggered by injection of a gas-rich andesitic magma batch at deep levels in the plumbing system.

To discriminate among the above hypotheses, we develop here a new protocol to accurately quantify the mass proportions of the different components in the tephra fall layer deposited west of the volcano. Pyroclastic fall deposits record many aspects of eruption phenomenology and the study of tephra distribution, thickness, grain-size and vesicularity has proved of utmost relevancy to infer the size, intensity and dynamics of explosive volcanic eruptions (Andronico et al., 2009; Arana-Salinas, et al., 2010; Bonadonna et al., 2002; Carey et al., 1995; Houghton et al., 2011; Miwa et al., 2009; Rose et al., 2008; Walker, 1973). Tephra studies are also increasingly used in the context of eruptive crises, notably at basaltic volcanoes (Andronico et al., 2008a, 2008b; Taddeucci et al., 2002, 2004). In particular, componentry analyses have great potential in deciphering eruption type, and magma–water and conduit processes (Arrighi et al., 2001; Carey et al., 2007; Carey and Houghton, 2010; Houghton et al., 2004; Rosi et al., 1999; Taddeucci et al., 2002). Yet, because of strong density variations in pyroclastic fall deposits (Sarna-Wojcicki et al., 1981), documenting the mass distributions of the components at the scale of the whole deposit is the most appropriate way to quantify the componentry proportions. While most recent studies focused on tephra volume calculation techniques (Biass and Bonadonna, 2011; Bonadonna and Costa, 2012; Bonadonna and Houghton, 2005; Fierstein and Nathenson, 1992, 1993; Pyle, 1989; Rose, 1993; Sulpizio, 2005), obtaining accurate estimates of the erupted mass has received much less attention. Most size determinations of explosive eruptions are based on volume-to-mass conversion using a single averaged or assumed value for the bulk density of the deposit (Carey et al., 2009; Costantini et al., 2009; Hill et al., 1998; Pioli et al., 2008; Sigurdsson and Carey, 1989). As a result, the detailed mass architecture of tephra fall deposits has remained poorly known and an insightful method to convert tephra volume to mass and determine the componentry mass distribution in a deposit is still lacking.

Here, we perform a high-resolution analysis of the eruptive mass budget, based on detailed quantitative investigations of componentry and mass distribution patterns in the 2006 Tungurahua tephra fall deposit. We show that the mass of the tephra layer is controlled by the proportion of each componentry class, which can be predicted from empirical laws evidenced for the first time in this work, and present an improved volume-to-mass conversion protocol to infer the size of the eruptive event. Our data highlight the influences of density-driven fractionation within the plume and clast packing on lateral mass distribution in the deposit. The results shed new lights on eruption dynamics and conduit processes at this dangerous volcano, and offer

valuable constraints on the origin of the August 2006 paroxysm that are of broad interest for the study of many other andesitic open-vent volcanoes worldwide.

## 2. Tungurahua volcano and the 2006 paroxysm

### 2.1. Geological background and recent ongoing activity

Tungurahua (5023 m a.s.l.) is a steep-sided andesitic strato-volcano located in the Eastern Andean Cordillera of Ecuador (Fig. 1A and B). It ranks as one of the most active volcanoes of the Northern Andes, with a recurrence rate of at least one pyroclastic flow-forming eruption per century (Hall et al., 1999; Le Pennec et al., 2008). More than 25,000 inhabitants live and cultivate lands on the flanks of the volcano and nearby areas, and are frequently threatened by lahars, ash falls, acid rains, and occasionally by pyroclastic flows.

The ongoing open-vent eruptive period, which started in 1999 after 80 years of repose, is characterised by a sub-persistent explosive activity of uneven intensity (low to moderate) and style, but also includes periods of quiescence and highly explosive paroxysmal phases, violent strombolian to subplinian in style (e.g. in November–December 1999, August 2001, July and August 2006, February 2008, May and December 2010, August 2012). The juvenile scoria products emitted during the whole eruptive period show homogeneous andesitic compositions (58–59 wt% SiO<sub>2</sub>; Samaniego et al., 2011).

### 2.2. The August 16–17, 2006 eruption

After several months of low-level activity in mid-2005, the activity progressively increased from December 2005 to June–July 2006. A first, rather modest pyroclastic flow-forming eruption took place on July 14th, with a 15 km-high tephra column. Several scoria flows went down the cone in gullies of the western flank, but most halted on the slopes. A fairly intense activity continued during the following weeks, with frequent ash emissions and strombolian explosions. On the morning of August 16th, the seismic activity increased rapidly. Sustained eruptive activity was witnessed in the afternoon and the first small-volume pyroclastic flows descended the north-west flank at 22:00 h UTC (UTC=local time+5 h). During the next few hours the eruptive activity increased progressively and the paroxysm occurred at about 05:15 h UTC on August 17th, and lasted around 50–60 min. Powerful and persistent incandescent lava jets attained more than 1 km above the crater and numerous pyroclastic flows rushed down to the base of the edifice (Kelfoun et al., 2009). A sustained eruption column rose more than 15 km above the summit, and the plume spread to the west above the Inter-Andean valley and the Pacific Ocean (Arellano et al., 2008; Eychenne et al., 2012; Kelfoun et al., 2009; Steffke et al., 2010). From 07:00 h UTC on August 17th, the eruptive activity decreased abruptly and andesitic lavas flowed down the western flank of the volcano and halted around 2700 m asl. Overall, the eruption lasted about 9 h, with 6 h of paroxysmal activity.

A bulk tephra volume in the range of 47–67 × 10<sup>6</sup> m<sup>3</sup> and a column height of 16–18 km above the vent has been estimated from ground-based studies (Eychenne et al., 2012), which ranks this eruption as VEI 3. Satellite remote sensing data point to a 19 km-high eruptive column (Steffke et al., 2010), which led Fee et al. (2010) to assign a VEI 4 for this eruptive phase.

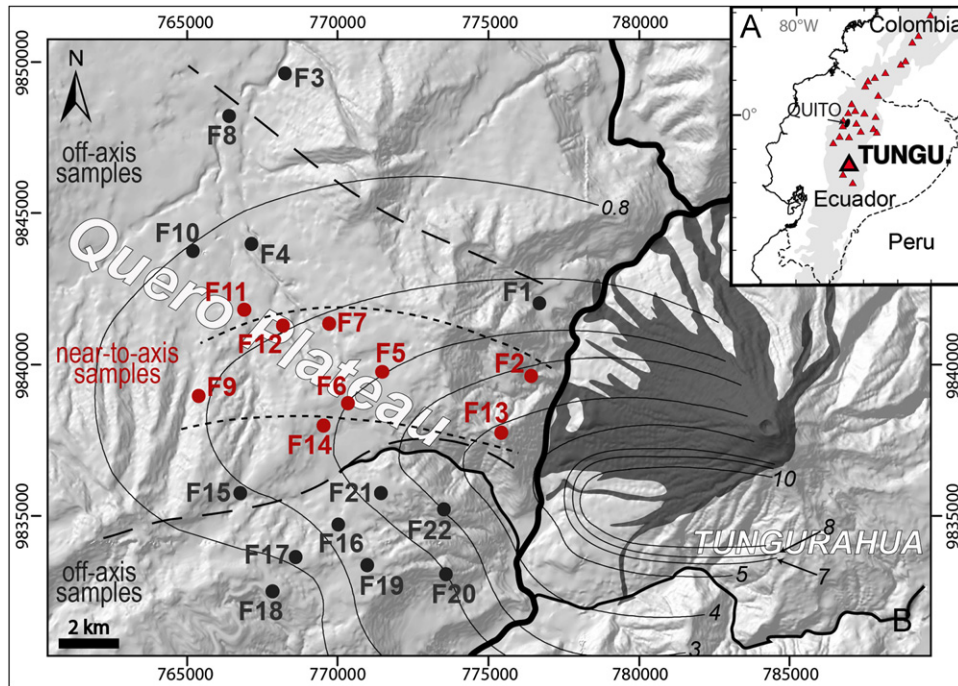


**Fig. 1.** (A) Location map of Tungurahua volcano in Ecuador. Greyed area: Andean relief above 2000 m a.s.l. Triangles: active volcanoes. (B) Area of sampling of the tephra fall deposit. Solid lines: isopach contours of the tephra fall layer after Eycheenne et al. (2012) (in cm). Dark area: depositional area of the pyroclastic density currents. Solid dots: sampling locations. Numerical labels: sample name. Red dots: “near-to-axis” samples. Black dots: “off-axis” samples. Area bounded by the dotted lines: area where  $x_{FS} > 40\%$ . Area bounded by the dashed lines: area where  $40 > x_{FS} > 20\%$  (after Eycheenne et al., 2012). (For interpretation of the references to colour in this figure legend, the reader is referred to the web version of this article.)

**Table 1**  
Summary of the notations used in this study.

Symbol	Definition (unit)
$a$	Area sampled ( $m^2$ )
$\alpha$	Constant parameter of the sigmoidal function
$\beta$	Constant parameter of the sigmoidal function
$i$	Grainsize in a half- $\phi$ scale
$j$	Componentry class (from S (Scoria class) to R (Reddish Scoria class))
$K$	Constant parameter of the sigmoidal function
$M$	Mass sampled (g)
$m_A$	Mass per unit area of particles in the samples ( $kg/m^2$ )
$m_{A_j}$	Mass per unit area of particles from the componentry class $j$ in the samples ( $kg/m^2$ )
$m_{A_{Calc}}$	Mass per unit area of particles in the samples calculated by addition of the mass per unit area of the different componentry classes ( $m_{A_j}$ ) ( $kg/m^2$ )
$Md\phi_{CS}$	Median diameter of the grain subpopulation in the fall deposit resulting from the sedimentation of tephra from the main eruptive plume ( $\phi$ )
$m_i$	Mass of particles in the grainsize fraction $i$ (g)
$M_j$	Mass of particles from the componentry class $j$ in the tephra fall deposit (kg)
$M_T$	Total mass of the tephra fall deposit (kg)
$\mu(i)$	Continuous function describing the variations of the mean particle density with $\phi$ in the samples
$\mu_p$	Mean particle density in the samples ( $kg/m^3$ )
$\phi$	Unit for grainsize calculated as $\phi = -\log_2 d$ , where $d$ is the particle diameter in (mm)
$\rho_b$	Bulk density of the deposit ( $kg/m^3$ )
$r$	Constant parameter of the sigmoidal function
$\sigma_{CS}$	Sorting of the grain subpopulation in the fall deposit resulting from the sedimentation of tephra from the main eruptive plume
$T$	Thickness of the deposit (cm)
$v_i$	Total particle volume in the grainsize fraction $i$ ( $m^3$ )
$v_{ij}$	Volume of particles in the componentry class $j$ of the grainsize fraction $i$ ( $m^3$ )
$V_b$	Bulk volume of deposit sampled ( $m^3$ )
$V_p$	Volume of particles in the samples ( $m^3$ )
$V_{IP}$	Volume of space between the particles (free inter-particle space) in the samples ( $m^3$ )
$x_{FS}$	Weight fraction of the fine subpopulation in the samples. This subpopulation has a mode around $4\phi$ and results from the sedimentation of fine particles from Co-PF clouds leading to bimodal grainsize distributions (Eycheenne et al., 2012).

### 3. The August 16–17, 2006 tephra fall deposit

#### 3.1. Depositional features and sampling

The tephra fall deposit occurred as a large fan west of the volcano, mainly on the Quero plateau, an area of the Inter-Andean

Valley located 7–20 km from the volcano (Fig. 1B). The isopach contours are sub-bilobate in shape and the tephra grain-size distribution is bimodal due to the synchronous deposition of coarse-grained lapilli and ash (from 30 mm to 90  $\mu m$ ) from the main plume and fine-grained ash ( $< 63 \mu m$ ) from co-pyroclastic flow clouds (Co-PF) (Eycheenne et al., 2012). At each sampling site

**Table 2**  
Key parameters of the samples (locations in Fig. 1B).  $x_{FS}$  and  $Md\phi_{CS}$  from Eychenne et al. (2012).

Sample	Thick. (cm)	Dist. (km)	$x_{FS}$ (wt%)	$Md\phi_{CS}$	$mA$ (kg/m <sup>2</sup> )	$\rho_b$ (kg/m <sup>3</sup> )	$\mu_p$ (kg/m <sup>3</sup> )	$V_b$ ( $\times 10^{-3}$ m <sup>3</sup> )	$V_p$ ( $\times 10^{-3}$ m <sup>3</sup> )	$V_m/V_b$ (%)
F1	3.79	8.5	21.6	−1.2	29.1	770	1970	1.50	0.59	60.9
F2	7.35	7.9	57.5	−2.0	100.2	1360	2170	2.93	1.84	37.2
F3	0.35	20.6	7.1	1.1	2.7	780	2230	0.15	0.05	65.0
F4	1.19	18.1	35.0	0.8	10.3	860	2280	0.47	0.18	62.0
F5	3.48	12.8	41.9	−0.1	37.2	1070	2190	1.39	0.68	51.1
F6	2.28	13.9	41.7	0.3	27.0	1190	2280	0.91	0.47	48.0
F7	2.25	14.9	40.6	0.0	25.9	1150	2280	0.90	0.46	49.4
F8	0.80	20.6	24.9	1.4	6.3	790	2390	0.32	0.10	67.1
F9	1.39	18.8	50.3	1.0	14.4	1040	2360	0.55	0.24	56.1
F10	0.71	19.9	29.6	0.7	6.7	940	2260	0.28	0.12	58.5
F11	1.35	17.7	35.4	0.8	13.8	1020	2270	0.54	0.24	54.8
F12	1.85	16.3	42.1	0.7	20.0	1080	2340	0.74	0.34	53.7
F13	5.00	8.8	46.2	−0.7	63.5	1270	2180	0.75	0.44	41.8
F14	2.04	14.7	21.5	0.2	22.4	1100	2300	0.81	0.39	52.1
F15	0.71	17.6	27.2	1.5	7.8	1100	2350	0.07	0.03	53.3
F16	1.43	14.6	19.1	0.7	13.4	940	2260	0.57	0.24	58.5
F17	0.84	16.2	22.7	1.3	7.0	830	2370	0.33	0.12	64.8
F18	0.64	17.3	25.2	1.5	5.0	790	2430	0.06	0.02	67.5
F19	1.10	14.1	14.2	0.4	9.3	840	2200	0.44	0.18	61.7
F20	1.81	11.7	12.0	0.1	15.4	850	2150	1.13	0.45	60.5
F21	1.80	12.9	19.0	0.2	17.0	940	2170	1.62	0.71	56.4
F22	2.95	11.0	14.1	−0.3	23.9	810	2090	4.13	1.60	61.3

(Fig. 1B), the weight fraction of the fine-grained ash subpopulation resulting from Co-PF clouds deposition is noted  $x_{FS}$  (all symbols used here and below are reported in Table 1). It varies laterally from more than 40% in the main depositional lobe, which coincides with downwind prolongation of the pyroclastic flows (PF) depositional area, to less than 20% in the secondary lobe and “wings” of the deposit (Fig. 1B; Table 2) (Eychenne et al., 2012).

The tephra fall deposit was sampled at 22 sites upon the Quero Plateau (Fig. 1B and Table 2). The sampling protocol consisted in separating and collecting a parallelepiped of known surface area  $a$  in the deposit from flat-lying surfaces. The thickness of the isolated portion was measured at the four corners and at each mid-point on the four sides, and the average was calculated.

### 3.2. Componentry and density data

Based on morphological and textural criteria, six main classes of particles were distinguished in the deposit (Fig. 2): (1) scoriae (S): ragged, dark to brown juvenile vesicular particles with homogeneous andesitic composition (57.6–58.9 wt% SiO<sub>2</sub>; Samaniego et al., 2011); (2) pumices (P): light-toned, highly vesicular juvenile clasts with a more siliceous composition (61.1–62.5 wt% SiO<sub>2</sub>; Samaniego et al., 2011), showing a glassy texture and sub-spherical vesicle shapes; (3) free crystals (C): mainly euhedral plagioclase and pyroxene, with irregular glass coating; (4) dense lithics (D): dark blocky, micro-crystalline non-vesicular clasts; (5) crystalline aggregates (A): assemblages of plagioclase and pyroxene crystals with little or no interstitial glass; (6) reddish scoriae (R): sub-rounded, moderately vesicular grains with cavities and vesicles, about 100–50  $\mu$ m in diameter, showing weathering and vapour-phase minerals on their surface. Ash aggregates and altered lithics were also identified (Fig. 2), but due to their paucity in the samples (< 0.01 wt%), they are not considered further in this study. Componentry analyses were carried out by grain identification and counting under the naked eye and the binocular microscope in all grainsize fractions  $\geq 90$   $\mu$ m of the 22 samples (Eychenne and Le Pennec, 2012) and the results are provided here as Electronic Supplementary data.

The particle density — ratio of the mass of a particle to its volume including the porosity — was measured in seven samples (F1, F2, F5, F7, F8, F11, F13 and F15; Fig. 1B). The results revealed a sigmoidal dependence of the mean particle density with grainsize

described by a function of the form (Eychenne and Le Pennec, 2012):

$$\mu(i) = K + \beta / (1 + \alpha e^{-ri}) \quad (1)$$

where  $i$  is the grainsize fraction on a  $\phi$ -scale (see Table 1 for  $\phi$  definition),  $\mu$  is the mean particle density and  $K$ ,  $\beta$ ,  $\alpha$  and  $r$  are constants. The parameters of Eq. (1) for the seven samples analysed are detailed in Table 1 of the Electronic Supplementary data.

These laws, along with the results of density measurements in scoria, pumice and dense lithic classes (the ranges of density values for the different components are compiled in Table 3), allow us to determine the mass per unit area of the different componentry classes in the grainsize fractions  $\geq 90$   $\mu$ m of the seven samples, by conversion of the results of the particle counting (Eychenne and Le Pennec, 2012).

## 4. Methodology

### 4.1. Determination of density and volume parameters

The sampling protocol (Section 3.1) allows us to determine the area and the bulk volume of the collected tephra ( $a$  and  $V_b$ , respectively). After drying in an oven at  $\sim 80$  °C for 12 h in the laboratory, the mass of the samples ( $M$ ) is measured to calculate the mass of tephra per unit area ( $mA = M/a$ ), and the bulk density of the deposit ( $\rho_b = M/V_b$ ). Using the sigmoidal law describing the variations of mean particle density with grainsize (Table 1 of the Electronic Supplementary data; Eychenne and Le Pennec, 2012), we calculate, for each sample, the total volume of particles ( $V_p = \sum m_i / \mu(i)$ ), the mean particle density ( $\mu_p = M/V_p$ ) and the volume of the free inter-particle space ( $V_{IP} = V_b - V_p$ ).

### 4.2. Mass calculation protocol

To assess the eruptive mass budgets of the August 2006 paroxysm, we develop a new protocol to calculate the total mass of each class of particles in the tephra fall deposit based on: (1) previously published componentry and particle density data (see Section 3.2; Eychenne and Le Pennec, 2012) and (2) the determination of the

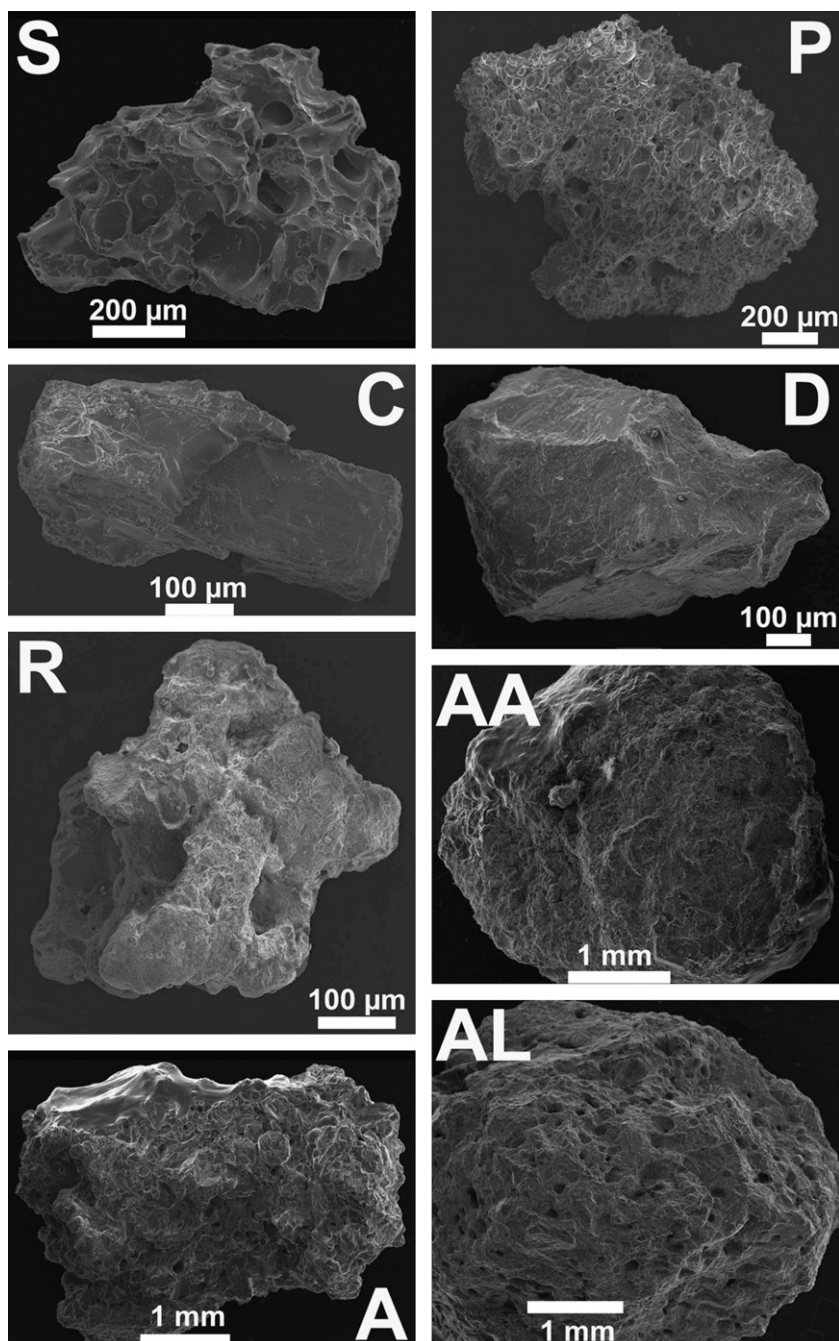


**Fig. 2.** Example of particles from the eight componentry classes identified in the August 2006 Tungurahua tephra fall layer: scoriae (S), pumices (P), free crystals (C), dense lithics (D), crystalline aggregates (A), red scoriae (R), ash aggregates (AA) and altered lithics (AL). Secondary electrons SEM images.

lateral mass distribution patterns of the different componentry classes.

Firstly, we extend the conversion protocol of the componentry data described in Eychenne and Le Pennec (2012) to the 15 other samples, using the sigmoidal density laws established for the seven analysed samples and assuming that the density distribution in non-analysed samples is similar to that of closest analysed ones in the same depositional area (Table 1 of the Electronic Supplementary data). Then, summing the componentry distributions in mass per unit area over the whole grainsize range, we calculate the mass per unit area of each componentry class ( $m_{Aj}$ ) in the 22 samples. These data are plotted on a map and iso-mass contours are designed for the six classes. The mass decay rates of each componentry class are plotted on a graph of  $m_{Aj}$  — the mass per unit area of each componentry

class — vs. square root of the iso-mass area ( $\sqrt{A}$ ). Using the relation between  $m_{Aj}$  and  $\sqrt{A}$  ( $m_{Aj} = f(\sqrt{A})$ ), the mass of the componentry class in the whole deposit ( $M_j$ ) is calculated by integration:

$$M_j = \int_0^{+\infty} m_{Aj} dA = \int_0^{+\infty} f(\sqrt{A}) dA \quad (2)$$

## 5. Results

### 5.1. Lateral mass and volume distributions in the deposit

The mass per unit area calculated for each sampling location ( $m_A$ ) occurs between 2.7 (sample F3) and 100.2 kg/m<sup>2</sup> (F2).

**Table 3**  
Mass and DRE volume of the six main componentry classes (P: Pumices, S: Scoriae, C: Free Crystals, D: Dense Lithics, A: Crystalline Aggregates and R: Red Scoriae). Particle density and solid density ( $\rho_s$ ) values after Eychenne and Le Penne (2012) — the particle density values are from pycnometry measurements in different grainsize fractions.

Class	Particle density (kg/m <sup>3</sup> )	Math. law	$M_j$ (kg)	$\rho_s$ (kg/m <sup>3</sup> )	$V_{DRE}$ (m <sup>3</sup> )	Proportions (vol%)
P	~1100 to ~2400	Exp. Law	6.90E+07	2400	2.87E+04	0.4
S	~1400 to ~2500	Exp. Law	1.74E+10	2500	6.96E+06	90.3
		Power Law	1.36E+10	–	–	–
C		Exp. Law	1.57E+09	2900	5.40E+05	7.0
D	~2700	Exp. Law	1.27E+08	2700	4.70E+04	0.6
A		Exp. Law	1.32E+08	2900	4.54E+04	0.6
R		Exp. Law	2.35E+08	2600	9.02E+04	1.2
TOTAL Exp. Law			1.95E+10		7.71E+06	100.0
TOTAL Power Law			1.57E+10		–	–

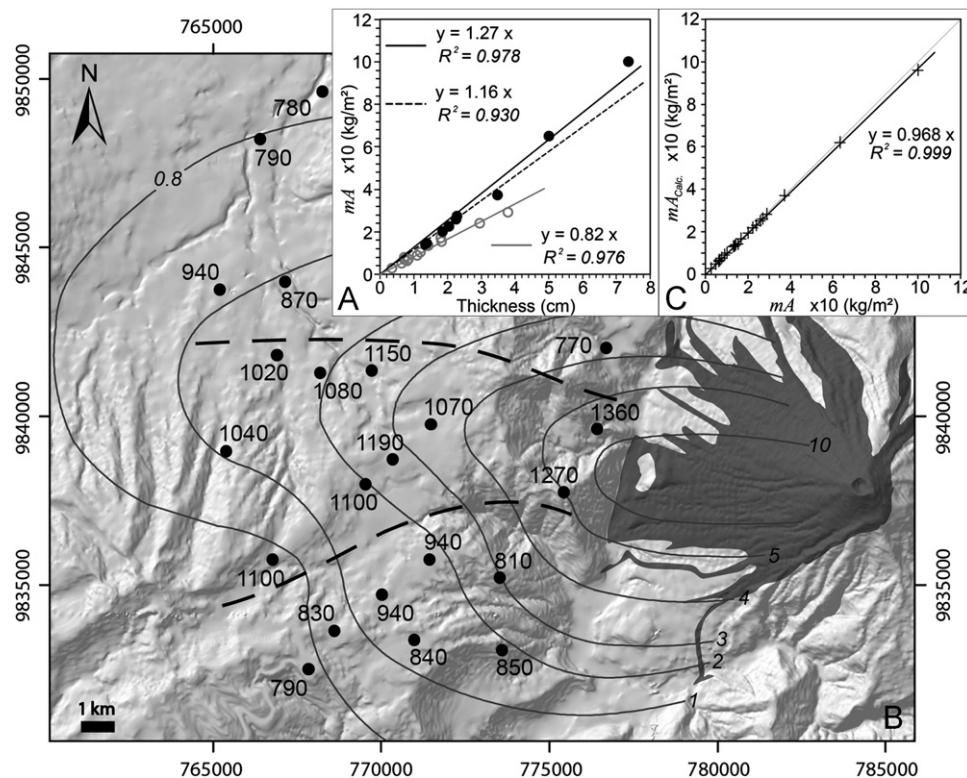


**Fig. 3.** (A) Plot of the mass per unit area ( $mA$ ) ( $\times 10 \text{ kg/m}^2$ ) vs. the thickness of the deposit (cm). Black and grey open dots are “near-to-axis” and “off-axis” samples, respectively, as defined in Fig. 1B. The solid, dashed and grey lines are regressions based on all, near-to, and off-axis data, respectively. (B) Bulk density ( $\text{kg/m}^3$ ) measured at each sampling location with isopach contours in cm indicated (solid curves). Dashed line: boundary of the area where  $\rho_b > 1000 \text{ kg/m}^3$ . (C) Plot of the reconstructed mass per unit area at each sampling location ( $mA_{calc}$ ) vs. the measured mass per unit area ( $mA$ ) ( $\times 10 \text{ kg/m}^2$ ). Grey line: straight line 1:1. Solid line: linear regression of the data.

$mA$  correlates linearly with thickness  $T$  ( $mA = 1.16 \times T$ ;  $R^2 = 0.93$ ) (Fig. 3A). The samples F2, F5–7, F9, and F10–14 collected close to the main dispersal axis of the plume (noted below “near-to-axis” samples, Fig. 1B), and those collected outside this area (referred to below as “off-axis” samples, Fig. 1B) line up on two straight lines (Fig. 3A).

The values for the bulk deposit density ( $\rho_b$ ) are between 770 and  $1360 \text{ kg/m}^3$  (Table 2). In the main depositional lobe,  $\rho_b$  is  $> 1000 \text{ kg/m}^3$  and decreases crudely away from the vent, from  $\sim 1400 \text{ kg/m}^3$  proximally to  $\sim 1000 \text{ kg/m}^3$  distally (Fig. 3B). The  $\rho_b$  data collected over the deposit, as a whole, show no correlation to the median diameter of the coarse-grained clast subpopulation (noted  $Md\phi_{CS}$ , Eychenne et al., 2012) (Fig. 4Aa and Table 2). Yet, along the main axis,  $\rho_b$  increases with median diameter, while off-axis,  $\rho_b$  remains constant (Fig. 4Aa).  $\rho_b$  increases with the weight percentage of fines ( $x_{FS}$ ) (Fig. 4Ab).

In all samples the mean particle density ( $\mu_p$ ) decreases with median diameter (Fig. 4Ba), but shows no correlation to the weight percentage of fines ( $x_{FS}$ ) (Fig. 4Bb). The free inter-particle space fraction (calculated as the ratio  $V_{IP}/V_b$  in %) decreases with median diameter and  $x_{FS}$  (Fig. 4Ca and b). At a similar grainsize, the proportion of free inter-particle space is higher for off-axis than near-to-axis samples (Fig. 4Ca).

## 5.2. Lateral mass distributions of the componentry classes

The mass per unit area of the componentry classes in each sample ( $mA_j$  for  $j$  from S to R) are reported on the maps of Fig. 5 and in Table 2 of the Electronic Supplementary data. To check for the relevancy of the conversion, we calculate the reconstructed masses per unit area ( $mA_{calc}$ ) by addition of  $mA_j$  of all the componentry classes in each sample. Fig. 3C shows that  $mA_{calc}$ .

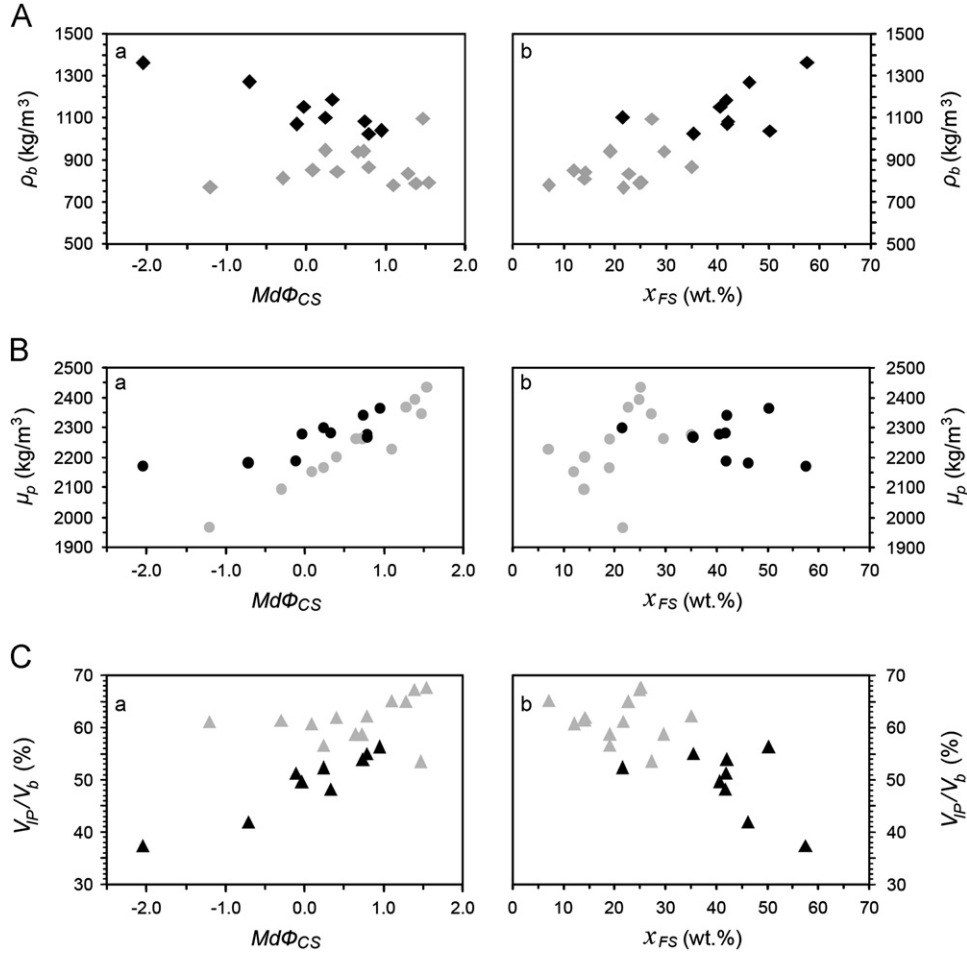


**Fig. 4.** Plots of the bulk deposit density ( $\rho_b$ ) (kg/m<sup>3</sup>) (A), the mean particle density ( $\mu_p$ ) (kg/m<sup>3</sup>) (B) and the proportion of inter-particle space ( $V_{IP}/V_b$  in %) (C), vs. the median diameter of the coarse grain-size sub-population of the deposit ( $Md\phi_{CS}$ ) (Phi scale) (a) and the fine-grained proportion ( $x_{FS}$ ) (wt%) (b). Solid markers: “near-to-axis” samples (Fig. 1B). Grey markers: “off-axis” samples (Fig. 1B).

is very similar to the mass per unit area inferred from bulk sample mass measurements ( $m_A$ , Table 2). This lends strong support to the validity of our conversion protocol.

Fig. 5 illustrates the distribution of mass per unit area of the six main componentry classes ( $m_{A_j}$ ). The shape of the iso-mass contours is linked to the nature of the componentry class (Fig. 5): (1) contours for free crystals (C), dense lithics (D) and crystalline aggregates (A) are fairly rounded, with an aspect ratio (major vs. minor axis) of 1.7, 1.3 and 1.6 respectively, (2) contours for scoriae (S), pumices (P), and reddish scoriae (R) are strongly elongated to the West, with ratios of 2.2, 2.3 and 3.0, respectively.

The plots of  $m_{A_j}$  vs. the square root of the iso-mass area ( $\sqrt{A}$ ) (Fig. 5) reveal that P, C, D, A and R data are well fitted by exponential laws, while S data are well fitted by a segmented exponential-law with two breaks in slope, or by a power law, of the forms:

$$m_{A_j} = m_{A_{j0}} \exp(-k\sqrt{A}) \quad (3)$$

$$m_{A_j} = m_{A_{jpl}} A^{-n/2} \quad (4)$$

where  $m_{A_{j0}}$  is the extrapolated mass per unit area at the vent,  $k$  is the slope of the exponential law,  $m_{A_{jpl}}$  and  $n$  are the power-law parameter and exponent, respectively (parameters and coefficient of determination  $R^2$  are reported in Fig. 5). The mass decay rates for the six componentry classes are compiled in Fig. 6, which reveal that D, A and C are characterised by the steepest decay rates.

### 5.3. Mass and volume of each componentry class

For the whole deposit the total mass of pumices ( $M_P$ ), free crystals ( $M_C$ ), dense lithics ( $M_D$ ), crystalline aggregates ( $M_A$ ) and red scoriae ( $M_R$ ) are calculated by integration of the exponential laws (Fig. 5), while the total mass of scoriae ( $M_S$ ) is determined by integration of the exponential law with two breaks-in-slope, and by integration of the power law (Fig. 5) from  $\sim 2$  km (calculated using the method of Bonadonna and Houghton, 2005) to 120 km (distance from the volcano to the Ecuadorian coast on an East–West parallel).  $M_S$  is  $1.74 \times 10^{10}$  kg and  $1.36 \times 10^{10}$  kg using exponential and power laws, respectively (Table 3).  $M_S$  is thus one order of magnitude higher than  $M_C$  ( $1.57 \times 10^9$  kg) (Table 3).  $M_D$ ,  $M_A$  and  $M_R$  ( $1.27 \times 10^8$ ,  $1.32 \times 10^8$ , and  $2.56 \times 10^8$  kg, respectively) are two orders of magnitude lower than  $M_S$ , while  $M_P$  ( $6.90 \times 10^7$  kg) is three orders of magnitude lower (Table 3). These masses are converted to Dense Rock Equivalent (DRE) volumes using, for each componentry class, solid density data ( $\rho_s$ ) from Eycheenne and Le Pennec (2012) (Table 3). The resulting DRE volumes range from  $7.0 \times 10^6$  m<sup>3</sup> for scoriae to  $2.9 \times 10^4$  m<sup>3</sup> for pumices (Table 3).

### 5.4. Magnitude and intensity

The total mass of the tephra fall deposit ( $M_T$ ) is calculated by summing the masses of the six componentry classes, which yields  $1.95 \times 10^{10}$  kg and  $1.57 \times 10^{10}$  kg using  $M_S$  from exponential and

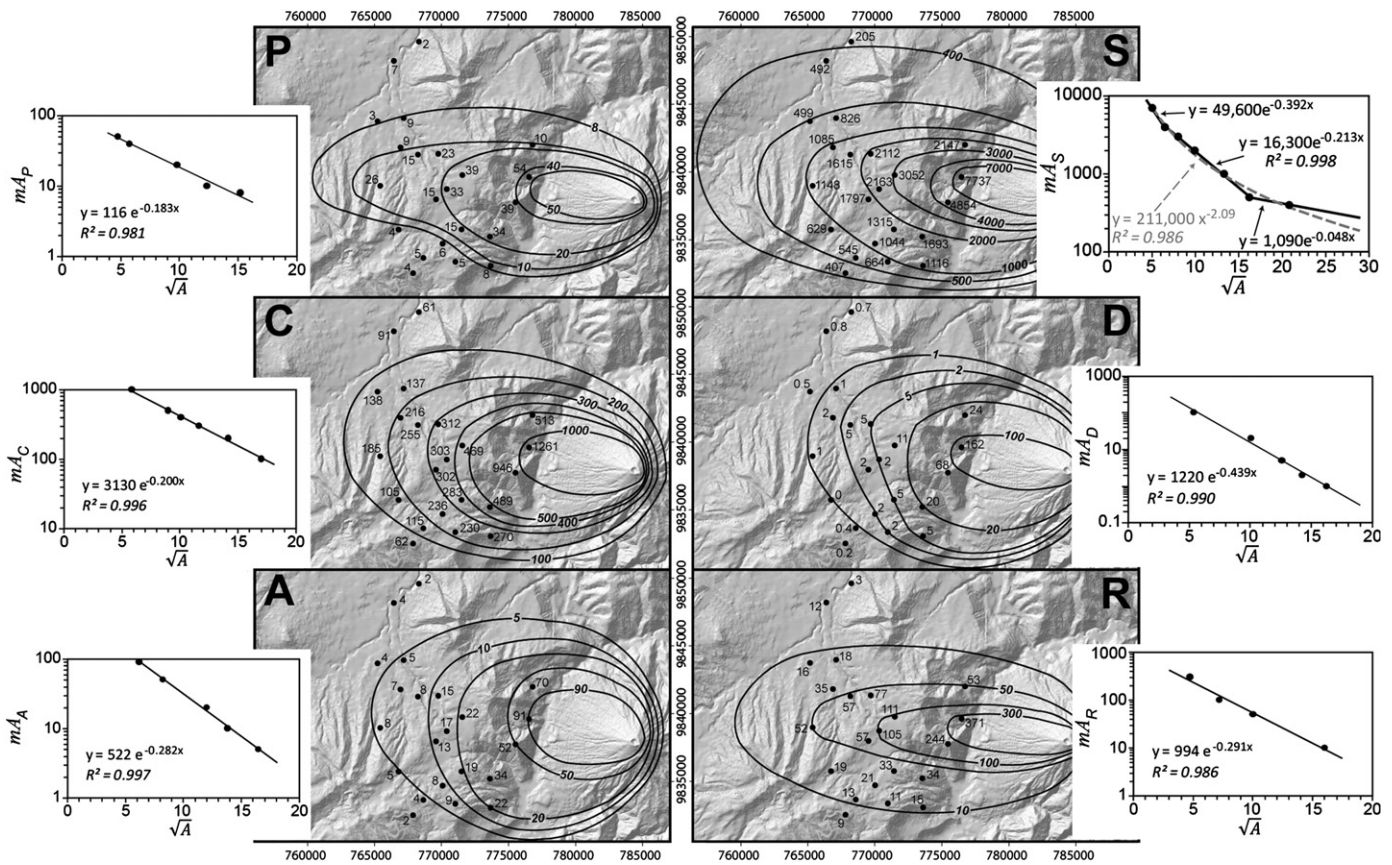


**Fig. 5.** Maps of the spatial distribution of the mass per unit area of the six major components of the deposit (P: Pumices, S: Scoriae, C: Free Crystals, D: Dense Lithics, A: Crystalline Aggregates and R: Red Scoriae). Numerical labels: values of the mass per unit area expressed as  $10^{-2}$  kg/m<sup>2</sup>. Solid curves: iso-mass lines. The insets represent the mass decay rates of the six components:  $m_j$  ( $\times 10^{-2}$  kg/m<sup>2</sup>) vs. the square root of the iso-mass area  $\sqrt{A}$  (km).

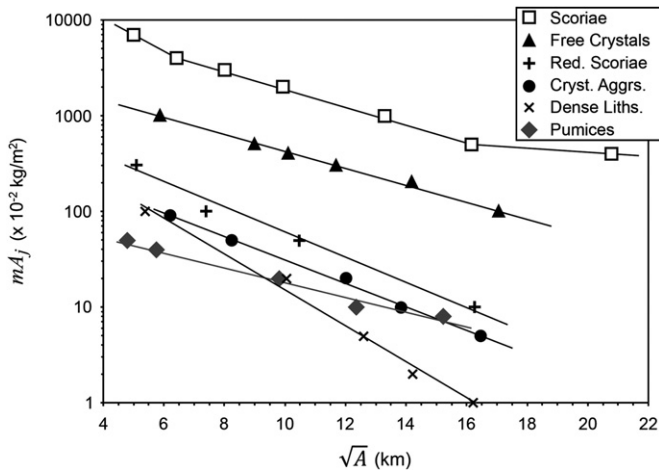


**Fig. 6.** Compilation of the mass decay rates of the six major components of the deposit. The straight lines represent the exponential fits of each set of data.

power laws, respectively (Table 3). In addition, we assessed  $M_T$  by converting the minimum bulk volume of the tephra fall deposit ( $42 \times 10^6$  m<sup>3</sup>; Eychenne et al., 2012), using a constant bulk deposit density. This density is difficult to constrain because of lateral variations. Here we use four bulk density data for conversion (Table 4): (1) the mean of the 22 bulk sample density measurements (980 kg/m<sup>3</sup>; Table 2); (2) the slope of the line correlating the mass per unit area to the thickness at each sampling location (1160 kg/m<sup>3</sup>; Fig. 3A); (3) the lowest and highest measured bulk densities (770 kg/m<sup>3</sup> at location F1, and

1360 kg/m<sup>3</sup> at location F2, respectively; Fig. 3B and Table 2). The calculated total masses  $M_T$  are  $4.1 \times 10^{10}$  kg,  $4.9 \times 10^{10}$  kg,  $3.2 \times 10^{10}$  kg and  $5.7 \times 10^{10}$  kg. Although these four results are of the same order of magnitude ( $10^{10}$  kg), the estimates vary in a 45% range.

Using the expression of Pyle (2000) (Magnitude =  $\log_{10}$ (erupted mass, kg) – 7), the eruption magnitude lies between 3.3 and 3.8 (Table 4). Considering 6 h of paroxysmal activity, the mean mass discharge rate of the August 2006 Tungurahua eruption is between  $0.9$  and  $2.7 \times 10^6$  kg/s, yielding an intensity between 9.0 and 9.4 (Table 4) (Intensity =  $\log_{10}$ (mass eruption rate, kg/s) + 3, Pyle, 2000). The total DRE volume obtained from componentry DRE volumes is  $7.7 \times 10^6$  m<sup>3</sup>, which translates into a DRE discharge rate (VER) of about 360 m<sup>3</sup>/s. Considering S, C, P and A as pure juvenile material, the VER of non-vesiculated magma is 350 m<sup>3</sup>/s.

## 6. Discussion

### 6.1. Mass distributions in the tephra fall deposit

The thinning rate of the 2006 Tungurahua deposit is described by an exponential law with two breaks-in-slope (Eychenne et al., 2012). Similar decay patterns are also documented at other tephra fall deposits worldwide, e.g. Askja 1875 (Carey et al., 2009), Novarupta 1912 (Bonadonna et al., 1998; Fierstein and Hildreth, 1992); Ruapehu 1996 (Bonadonna and Houghton, 2005). Bonadonna et al. (1998) proposed that the segmentation of the thinning rate results from different air-flow regimes (i.e. laminar vs. turbulent), which control proximal and distal sedimentation

**Table 4**

Magnitude and intensity of the eruption, considering an eruption duration of 6 h, determined for five different total mass of the tephra layer calculated by: (1) conversion using the mean of the 22 bulk density measurements performed over the deposit ( $980 \text{ kg/m}^3$ ; Table 2); (2) conversion using the slope of the line linking the mass per unit area to the thickness at each sampling location ( $1160 \text{ kg/m}^3$ ; Fig. 3A in SEM); (3) conversion using the lowest bulk density measured ( $770 \text{ kg/m}^3$  at location 1; Table 2), (4) conversion using the highest bulk density measured ( $1360 \text{ kg/m}^3$  at location 2; Table 2) and (5) addition of the componentry mass (Table 3).

	1	2	3	4	5
<b><math>M_j</math> (kg)</b>	4.11E+10	4.87E+10	3.23E+10	5.72E+10	1.95E+10
<b>Magnitude</b>	3.6	3.7	3.5	3.8	3.3
<b>Mass eruption rate (kg/s)</b>	1.90E+06	2.26E+06	1.49E+06	2.65E+06	9.04E+05
<b>Intensity</b>	9.3	9.4	9.2	9.4	9.0

patterns. Our results show that the shape of the Scoria mass decay rate (Fig. 5) is similar to the overall thinning rate of the deposit (Eychenne et al., 2012), because of dominant scoriae abundance. The breaks-in-slope occur at similar distances: at  $\sim 6\text{--}7 \text{ km}$  and at  $\sim 16\text{--}17 \text{ km}$  from the vent (Fig. 5). Thus, the sedimentation of the Scoriae clast population controls the segmentation pattern of the 2006 Tungurahua fall deposit thickness.

As far as we know, the lateral distribution of particle density has not been documented in previous works. Here we demonstrate that the mean particle density ( $\mu_p$ ) broadly decreases with median diameter (Fig. 4B) — i.e. toward the vent — a result which seems counterintuitive. At each sampling location, the mean particle density varies with grain size along a sigmoidal trend, which reflects increasing scoriae vesicularity with grain size (Eychenne and Le Pennec, 2012). Therefore, because grain sorting improves away from vent as median grain size decreases (Eychenne et al., 2012), distal samples contain dominantly dense particles. Consequently, the mean particle density increases with distance and its variations at the scale of the whole deposit are controlled by grain size distributions.

## 6.2. Clast packing

The above results on volume and mass distributions bring valuable information on clast arrangement and packing, and on lateral bulk density distribution in the deposits, an issue that has been rarely documented in previous volcanological studies (Sarna-Wojcicki, et al., 1981; Sheridan and Ragan, 1976). Complex lateral variations of the bulk density ( $\rho_b$ ) in the 2006 Tungurahua deposit (see Section 5.1) likely result from the interplay of several processes. Fig. 4Ca suggests that the proportion of free inter-particle space in the deposit increases with  $\phi$  and thus with distance. This is interpreted here as an effect of different particle packing. In proximal areas the deposit is coarse grained ( $-2 < Md\phi_{CS} < 0\phi$ ) and moderately to well sorted ( $1.5 < \sigma_{CS} < 2.0$ , Eychenne et al., 2012), a combination of factors that favours a dense packing, with small inter-particle space. In finer, more distant deposits, the sorting improves ( $\sigma_{CS} < 1.0$ ) resulting in a looser grain packing. These findings imply that the amount of free inter-particle space has a stronger impact on bulk tephra density than the mean particle density, a significant result that has never been reported before, to our knowledge.

We note in Fig. 4Ca that near-to- and off-axis samples plot along two sub-parallel trends, which suggests that packing is denser near-to- than off-axis. Examination of the map in Fig. 1B reveals that the weight fraction of fine-grained ash which settled from the Co-PF clouds ( $x_{FS}$ ) is the highest ( $> 40\%$ ) below the main dispersal axis. In this area, we interpret that the high amount of fine-grained particles from Co-PF clouds filled the free space between the lapilli which fell down from the main tephra plume, leading to denser grain packing. Conversely, packing is loose in areas uncontaminated by Co-PF ash, i.e. out of the main dispersal axis. This effect accounts for the different bulk density trends near-to- and off-axis (Fig. 4Aa). These results highlight the

significant influence of the sedimentation of Co-PF particles on bulk density distribution in a tephra fall deposit. Mass conversion of the volume of pyroclastic fall deposits from subplinian to plinian eruptions accompanied by Co-PF clouds — e.g. at Montserrat (Bonadonna et al., 2002), Volcan de Fuego (Rose et al., 2008), Colima (Evans et al., 2009) — can thus be highly misleading when the dispersal area of Co-PF cloud coincides with that of the main tephra cloud. With the bulk density value used above for the volume-to-mass conversion, the error on the mass estimate can be as high as 45% (Table 4). Therefore, applying this conversion method to strongly heterogeneous deposits (e.g. affected by aggregations processes, Co-PF ash contamination) can lead to large over- or under-estimation of the mass of tephra deposits.

## 6.3. Density-driven particle fractionation within the plume

Previous physical models of tephra dispersion and sedimentation have considered grain size- over density-driven fractionation (Bonadonna et al., 1998; Carey and Sparks, 1986; Rose, 1993; Sparks et al., 1992, 1997; Walker et al., 1971). Our results show, however, that density fractionation is an essential process which depends on the initial componentry classes in the emitted products. The effect of this process on mass distributions in tephra fall deposits has not been addressed thoroughly in previous studies. Studies of maximum size of pumices and lithics in tephra fall deposits (e.g. Nawotniak and Bursik, 2010; Pistolesi et al., 2011; Pyle, 1989; Rosi et al., 1999; Rossotti et al., 2006; Walker, 1980) have shown that pumice clasts are transported further away than lithics of similar size, evidencing higher pumice floatability due to a lower density. Detailed componentry analysis of the May 18th, 1980 Mount St. Helens tephra deposit illustrates a general increase of pumices and glass shard vs. crystals and lithics fractions away from vent (Carey and Sigurdsson, 1982). Our results (Figs. 5 and 6) reveal that the componentry density controls the shape of the iso-mass contours and the mass decay rate, thus evidencing different mass-dependant dispersion patterns within the plume. The westward elongated iso-mass curves of Scoriae, Pumices and Red scoriae point out a strong effect of the wind, while this latter is weaker for free Crystals, crystalline Aggregates and Dense lithics, as indicated by sub-circular iso-mass contours (Fig. 5). High-density clasts are thus less influenced by wind during transport in the umbrella cloud than light particles (Pumices and Scoriae). Furthermore, the mass decay rates of the densest components (C, D, A) are steeper than those of S, P and R (Fig. 6). These results illustrate different sedimentation behaviours owed to their dissimilar floatability, leading to a fractionation process of each componentry class within the plume and to uneven lateral mass distribution of the components within the deposit. These findings yield a much more detailed view of tephra layer structure than the classical maximum pumice and lithic sizes, whose deposition may be partly influenced by ballistic transport, resulting in more circular isopleth contour shape

(Rossotti et al., 2006; Walker, 1980; Walker and Croasdale, 1971). Our approach brings a high-resolution perspective of componentry and mass distribution at the scale of the proximal and median deposits at an unprecedented level of detail, and demonstrates that density-driven fractionation processes within the plume needs to be better accounted for numerical modelling of tephra dispersion.

#### 6.4. Magnitude and intensity of the August 2006 eruption

With Pyle's (2000) definitions, our results point to a mass magnitude of  $\sim 3.6$  and an intensity of  $\sim 9.2$ , and thus a VER of magma of about  $350 \text{ m}^3/\text{s}$ . Calculations using broader input data (Table 4) suggest that these values are accurate within a range of 0.3 for magnitude and 0.2 for intensity. These results are consistent with a VEI of 3, as inferred from tephra volume estimates (Eychenne et al., 2012), and differ from the VEI 4 inferred from satellite-based plume height monitoring (Fee et al., 2010; Steffke et al., 2010). The calculated magnitude and intensity are significantly higher than those of typical violent Strombolian eruptions characterised by intensities between 7 and 8 (Arrighi et al., 2001; Pioli et al., 2008; Pyle, 2000), and rather support a Subplinian style, with magnitudes of 4 and intensities in the ranges of 9–10 (Arrighi et al., 2001; Bower and Woods, 1996; Cioni et al., 2000). For comparison, the August 2006 Tungurahua eruption is similar in magnitude and intensity to the 1992 Subplinian eruptions of Mount Spurr volcano, Alaska (magnitude  $\sim 3.6$  and intensity  $\sim 9.4$ ; McGimsey et al., 2001), and weaker than typical Plinian eruptions like those of Mount Pinatubo in 1991 (magnitude  $\sim 6$  and intensity  $\sim 11.6$ ) and Mount St. Helens in 1980 (magnitude  $\sim 4.8$  and intensity  $\sim 10.3$ ) (Pyle, 2000). However, the 2006 Tungurahua paroxysm plots as Plinian (Eychenne et al., 2012) in current classification schemes which are based on dispersion-fragmentation parameters (Pyle, 1989; Walker, 1973). This discrepancy between eruptive type inferred from dispersal and grainsize data, and mass-based eruption type appraisal, suggests that current classification schemes might need to be revisited on mass-based scales.

This relatively high magnitude makes the 2006 event as the most explosive and violent phase of the ongoing eruptive period at the time we write. The size of the August 2006 event is seemingly similar to that of past millennium eruptions (Le Pennec et al., 2008), but significantly smaller than some pre-Columbian andesitic and dacitic events, as those of  $\sim 1.2 \text{ ka BP}$  and  $\sim 3 \text{ ka BP}$  (Hall et al., 1999; Le Pennec et al., 2006). Yet, our results incorporate neither the amount of ballistic tephra deposits, whose influence on overall mass and magnitude determinations is significant at Tungurahua and other volcanoes (e.g. Le Pennec et al., 2012; Valade and Donnadieu, 2011), nor that of PF deposits ( $5\text{--}10 \times 10^6 \text{ m}^3$  according to Hall et al., 2007 and Kelfoun et al., 2009) and lavas ( $\sim 7 \times 10^6 \text{ m}^3$ ). These limitations illustrate the difficulty to obtain accurate eruption magnitude and intensity indexes for complex eruptions (e.g. including lava flows, PF, tephra falls and ballistics) when the determination is based solely on volume and mass estimates of tephra fall deposits.

The discrepancy between the total mass ( $M_T$ ) obtained from conversion of the bulk tephra layer volume and from the sum of each component mass ( $\sum M_j$ ) raises questions about the mass determination method. This difference, which varies from 1.3 to  $3.8 \times 10^6 \text{ kg}$  (Table 4), might be due to the difficulty in setting a constant value of the bulk density for the conversion, although the lowest measured density ( $770 \text{ kg/m}^3$ ) yields a total mass still 0.6 times higher than  $M_T$  calculated as  $\sum M_j$ . The bulk volume is calculated using the same integration method as  $M_j$  (Eychenne et al., 2012). Yet, while the thickness decay rate is known as far as 60 km (because some thickness measurements were obtained

beyond the sampling area; Eychenne et al., 2012), the mass decay rates are not documented beyond 20 km (Figs. 5 and 6), leading to underestimate the total tephra mass when calculated as  $\sum M_j$ , notwithstanding the distal ash particles are denser on average (Fig. 4Ba).

#### 6.5. Triggering mechanism of the August 2006 paroxysm

One main goal of our study is to decipher the origin of sudden strongly explosive events at open-system andesitic volcanoes. The mass decay rates allow us to unfold density-driven fractionation effects at the scale of the whole layer, and to infer high-resolution eruptive mass budgets of each componentry class at the vent. This brings relevant insights to pinpoint the cause of the August 2006, pyroclastic flow-forming paroxysm at Tungurahua. The mass fraction of silicic pumice clasts is much too small ( $< 0.4\%$  of total juvenile mass — very small proportion which contrasts with the apparent high quantity appraised at first sight in the field soon after the eruption) to explain the elevated August 2006 explosivity by massive magma mixing at depth in the system, in a context of open-vent behaviour since 1999. On the other hand, the high juvenile content (98% of the erupted mass; Table 3) and the density distribution patterns of the juvenile fraction (Eychenne and Le Pennec, 2012) point to a violent eruptive style essentially driven by magmatic processes. This is consistent with the modest mass fraction of xenolithic materials (1.8% of the total mass; Table 3), which suggests minor or no magma–water interaction contributing to the explosivity (Heiken and Wohletz, 1985; Taddeucci et al., 2002). This is also supported by the progressive increase of the eruption intensity during several hours before culminating in the pyroclastic flow-forming paroxysm. Altogether, our results lend support to those of the petrological investigation (Samaniego et al., 2011), and depict the ongoing Tungurahua activity as an andesitic open-system frequently fed by injections of deep magma batches that rise to the surface on a timescale of weeks to a few months. Gas-rich batches of larger size are highly mobile and their rapid ascent and intense fragmentation can cause enhanced erosion of the upper conduit, and trigger violent eruptive styles at the vent (Scandone et al., 2007). Such intermittent deep magma recharges have been evidenced at Arenal to explain its unsteady sub-continuous activity (Streck et al., 2002). The 2006 Tungurahua paroxysm should thus be regarded as an extreme event in the continuous size-frequency spectra of the successive eruptive phases witnessed since 1999.

#### 6.6. Conduit processes inferred from componentry masses

The componentry mass estimates offer relevant information on the shallow plumbing system and conduit processes, which have remained poorly known at andesitic open systems, and notably at Tungurahua. In the context of the 2006 event, the silicic pumice fraction (Table 3) might represent an isolated body of cooling and crystallising, possibly non-eruptible magma stocked at depth as a small-size residual batch from previous historical or pre-historical eruptions. The rapidly ascending 2006 magma batch would have remobilised this differentiated magma pocket. This suggests that the entrainment potential of the August 2006 rising magma batch was much higher than that of previous recharges which fed the intermittent open-vent activity at Tungurahua since 1999 (Samaniego et al., 2011), and this may be related to a higher magma ascent rate (Wright et al., 2012).

The colour and surface texture of the Reddish Scoriae suggest an origin from the hydrothermal system surrounding the active conduit. This componentry class has been frequently reported in Tungurahua's ash fall deposits since the beginning of the

magmatic activity in 1999, although in fairly limited proportions (e.g.  $\sim 4$  vol% in the August 2001 ash fall layer; Le Pennec et al., 2012). The dark angular lithics have not been described prior to the 2006 eruption. We propose that these unaltered xenoclasts were incorporated during eruption from erosion of conduit walls inside the volcanic edifice, suggesting that the intensity and erosive power of the event were high enough to carve unaltered wall-rocks further than the pre-existing active conduit walls, which are hydrothermally more altered. The absence of xenoclastic material from the metamorphic basement, which is known from geological studies and seismic tomography data to rise up to  $\sim 3$  km a.s.l. inside the volcano (Molina et al., 2005), implies that magmatic fragmentation and conduit erosion occurred essentially in the upper  $\sim 2$  km of the plumbing system. Seismological monitoring in the course of the ongoing eruptive period reveals that most long period events have their sources located along a narrow vertical pipe below the crater (Kumagai et al., 2011). Given the DRE volume of non-juvenile products (D and R:  $1.5 \times 10^5 \text{ m}^3$ ) and assuming a 2 km-high, 10 m-radius cylinder-shaped conduit (diameter estimated from repeated airborne observations of the active vent inside Tungurahua's crater) and uniform erosion rate over the whole length of the conduit, yields a mean erosion velocity of  $8.6 \times 10^{-5} \text{ m/s}$  (i.e. 31 cm/h) for the 6 h-long paroxysm. It is likely, however, that erosion occurred chiefly in the very upper levels of the conduit where fragmentation and jet ejection occurred (e.g. Carey and Houghton, 2010; Fierstein et al., 1997).

## 7. Conclusion

A detailed investigation of the August 2006 Tungurahua deposit reveals the subtle mass distribution architecture of a scoria fall layer, and brings new lights on the origin of a subplinian event at an open-vent, andesitic volcano. Our high-resolution analysis of tephra dispersal and weight distributions documents regular componentry-dependant mass decay rates, which allows integration over wide areas and size ranges. In comparison to classical volume-to-mass conversions obtained using a single bulk deposit density, our mass budget analysis yields improvements for magnitude–intensity estimation and a significantly different view of eruption processes, as it accounts for uneven density distribution in the deposit. It also yields evidence of complex and subtle controls of componentry proportions, clast packing patterns, and fractionation processes on actual lateral mass distribution in a typical scoria fall layer. In addition, it is applicable in the context of eruptive crises, as it allows with a few reasonable assumptions rapid and fairly accurate mass and eruption size determinations, without requiring heavy instrumental deployment or close approach to the active vents.

As a result, we show that the August 2006 eruptive paroxysm at Tungurahua is the consequence of a voluminous, gas-rich magma recharge at depth that rapidly ascended to the surface, while the volcano was already erupting under open-vent behaviour. These conclusions raise concerns in terms of volcano monitoring at Tungurahua because such infrequent but dangerous paroxysms are not preceded by clear geophysical and geochemical precursors, whose interpretation is usually difficult at continuously active systems. Notably, the deep origin of this eruptive behaviour poses serious worries in terms of evacuation decision in areas where populations are threatened by potential pyroclastic flows. These outcomes are most likely applicable to other hazardous explosive andesitic edifices worldwide, where strong eruptive phases occur during long-lived mild intensity eruptions (Colima in Mexico, Sakurajima in Japan, Arenal in Costa-Rica, Merapi and Semeru in Indonesia, and Sangay in

Ecuador) and elsewhere. They should motivate future research to get better understanding of volcanic processes and to identify potential precursors of sudden violent eruptive phases at permanently active andesitic volcanoes.

## Acknowledgements

This work is part of a PhD project by J. Eychenne and has been financially supported by a project entitled “Volcanic hazards associated with open-system activity” (Action Incitative of IRD). This research has been completed in the context of a Laboratoire Mixte International “Séismes et Volcans dans les Andes du Nord”, which links the Instituto Geofísico of Quito's polytechnic school to three research entities in France, including the Laboratoire Magmas et Volcans of Blaise Pascal University, Clermont II. L. Gailler and A. Delcamp carried out a great part of the tedious grain counting and pycnometry analysis, and are warmly acknowledged. The authors thank C. Bonadonna and J.-C. Komorowski for discussions and comments on an early version of this paper. Insightful corrections and comments by two anonymous reviewers and editorial handling by B. Marty enhanced the quality of this paper. This is Laboratory of Excellence ClerVolc contribution no. 44.

## Appendix A. Supporting information

Supplementary data associated with this article can be found in the online version at <http://dx.doi.org/10.1016/j.epsl.2012.11.002>.

## References

- Alvarado, G.E., Soto, G.J., 2002. Pyroclastic flow generated by crater-wall collapse and outpouring of the lava pool of Arenal Volcano, Costa Rica. *Bull. Volcanol.* 63, 557–568.
- Andronico, D., Cristaldi, A., Scollo, S., 2008a. The 4–5 September 2007 lava fountain at South-East Crater of Mt Etna, Italy. *J. Volcanol. Geotherm. Res.* 173, 325–328.
- Andronico, D., Scollo, S., Cristaldi, A., Caruso, S., 2008b. The 2002–03 Etna explosive activity: tephra dispersal and features of the deposit. *J. Geophys. Res.* 113, B04209.
- Andronico, D., Scollo, S., Cristaldi, A., Ferrari, F., 2009. Monitoring ash emission episodes at Mt Etna: the 16 November 2006 case study. *J. Volcanol. Geotherm. Res.* 180, 123–134.
- Arana-Salinas, L., Siebe, C., Macías, J.L., 2010. Dynamics of the ca. 4965 yr 14C BP “Ochre Pumice” Plinian eruption of Popocatepetl volcano, México. *J. Volcanol. Geotherm. Res.* 192, 212–231.
- Arellano, S., Hall, M., Samaniego, P., Le Pennec, J.-L., Ruiz, A., Molina, I., Yepes, H., 2008. Degassing patterns of Tungurahua volcano (Ecuador) during the 1999–2006 eruptive period, inferred from remote spectroscopic measurements of  $\text{SO}_2$  emissions. *J. Volcanol. Geotherm. Res.* 176, 151–162.
- Arrighi, S., Principe, C., Rosi, M., 2001. Violent strombolian and subplinian eruptions at Vesuvius during post-1631 activity. *Bull. Volcanol.* 63, 126–150.
- Biass, S., Bonadonna, C., 2011. A quantitative uncertainty assessment of eruptive parameters derived from tephra deposits: the example of two large eruptions of Cotopaxi volcano, Ecuador. *Bull. Volcanol.* 73, 73–90.
- Bonadonna, C., Ernst, G.G.J., Sparks, R.S.J., 1998. Thickness variations and volume estimates of tephra fall deposits: the importance of particle Reynolds number. *J. Volcanol. Geotherm. Res.* 81, 173–187.
- Bonadonna, C., Mayberry, G.C., Calder, E.S., Sparks, R.S.J., Choux, C., Jackson, P., Lejeune, A.M., Loughlin, S.C., Norton, G.E., Rose, W.I., Ryan, G., Young, S.R., 2002. Tephra fallout in the eruption of Soufrière Hills Volcano, Montserrat. In: Druitt, T.H., Kokelaar, B.P. (Eds.), *The Eruption of Soufrière Hills Volcano, Montserrat, from 1995 to 1999*, vol. 21. Geological Society, London, *Memoirs*, pp. 483–516.
- Bonadonna, C., Houghton, B.F., 2005. Total grain-size distribution and volume of tephra-fall deposits. *Bull. Volcanol.* 67, 441–456.
- Bonadonna, C., Costa, A., 2012. Estimating the volume of tephra deposits: a new simple strategy. *Geology* 40, 415–418.
- Bower, S.M., Woods, A.W., 1996. On the dispersal of clasts from volcanic craters during small explosive eruptions. *J. Volcanol. Geotherm. Res.* 73, 19–32.
- Camus, G., Gourgaud, A., Mossand-Berthommier, P.-C., Vincent, P.-M., 2000. Merapi (Central Java, Indonesia): an outline of the structural and

- magmatological evolution, with a special emphasis to the major pyroclastic events. *J. Volcanol. Geotherm. Res.* 100, 139–163.
- Carey, S., Sigurdsson, H., 1982. Influence of particle aggregation on deposition of distal tephra from the May 18, 1980, eruption of Mount St. Helens volcano. *J. Geophys. Res.* 87, 7061–7072.
- Carey, S., Sparks, R.S.J., 1986. Quantitative models of the fallout and dispersal of tephra from volcanic eruption columns. *Bull. Volcanol.* 48, 109–125.
- Carey, S., Gardner, J., Sigurdsson, H., 1995. The intensity and magnitude of Holocene plinian eruptions from Mount St. Helens volcano. *J. Volcanol. Geotherm. Res.* 66, 185–202.
- Carey, R.J., Houghton, B.F., Sable, J.E., Wilson, C.J.N., 2007. Contrasting grain size and componentry in complex proximal deposits of the 1886 Tarawera basaltic Plinian eruption. *Bull. Volcanol.* 69, 903–926.
- Carey, R.J., Houghton, B.F., Thordarson, T., 2009. Tephra dispersal and eruption dynamics of wet and dry phases of the 1875 eruption of Askja Volcano, Iceland. *Bull. Volcanol.* 72, 259–278.
- Carey, R.J., Houghton, B.F., 2010. "Inheritance": an influence on the particle size of pyroclastic deposits. *Geology* 38, 347–350.
- Charbonnier, S.J., Gertisser, R., 2008. Field observations and surface characteristics of pristine block-and-ash flow deposits from the 2006 eruption of Merapi Volcano, Java, Indonesia. *J. Volcanol. Geotherm. Res.* 177, 971–982.
- Cioni, R., Marianelli, P., Santacroce, R., Sbrana, A., 2000. Plinian and subplinian eruptions. In: Sigurdsson, H. (Ed.), *Encyclopedia of Volcanoes*. Academic Press, New York, pp. 477–494.
- Cole, P.D., Fernandez, E., Duarte, E., Duncan, A.M., 2005. Explosive activity and generation mechanisms of pyroclastic flows at Arenal volcano, Costa Rica between 1987 and 2001. *Bull. Volcanol.* 67, 695–716.
- Costantini, L., Bonadonna, C., Houghton, B., Wehrmann, H., 2009. New physical characterization of the Fontana Lapilli basaltic Plinian eruption, Nicaragua. *Bull. Volcanol.* 71, 337–355.
- Evans, J.R., Huntoon, J.E., Rose, W.I., Varley, N.R., Stevenson, J.A., 2009. Particle sizes of andesitic ash fallout from vertical eruptions and co-pyroclastic flow clouds, Volcan de Colima, Mexico. *Geology* 37, 935–938.
- Eychenne, J., Le Pennec, J.L., 2012. Sigmoidal particle density distribution in a subplinian scoria fall deposit. *Bull. Volcanol.* 74, 2243–2249.
- Eychenne, J., Le Pennec, J.L., Troncoso, L., Gouhier, M., Nedelec, J.M., 2012. Causes and consequences of bimodal grain size distribution of tephra fall deposited during the August 2006 Tungurahua eruption (Ecuador). *Bull. Volcanol.* 74, 187–205.
- Fee, D., Garces, M., Steffke, A., 2010. Infrasonic from Tungurahua Volcano 2006–2008: Strombolian to Plinian eruptive activity. *J. Volcanol. Geotherm. Res.* 193, 67–81.
- Fierstein, J., Nathenson, M., 1992. Another look at the calculation of fallout tephra volumes. *Bull. Volcanol.* 54, 156–167.
- Fierstein, J., Hildreth, W., 1992. The plinian eruptions of 1912 at Novarupta, Katmai National Park, Alaska. *Bull. Volcanol.* 54, 646–684.
- Fierstein, J., Nathenson, M., 1993. Reply to comment by W.I. Rose. *Bull. Volcanol.* 55, 375–378.
- Fierstein, J., Houghton, B.F., Wilson, C.J.N., Hildreth, W., 1997. Complexities of plinian fall deposition at vent: an example from the 1912 Novarupta eruption (Alaska). *J. Volcanol. Geotherm. Res.* 76, 215–227.
- Gertisser, R., Keller, J., 2003. Temporal variations in magma composition at Merapi (Central Java, Indonesia): magmatic cycles during the past 2000 years of explosive activity. *J. Volcanol. Geotherm. Res.* 123, 1–23.
- Gertisser, R., Charbonnier, S.J., Troll, V.R., Keller, J., Preece, K., Chadwick, J.P., Barclay, J., Herd, R.A., 2011. Merapi (Java, Indonesia): anatomy of a killer volcano. *Geol. Today* 27, 57–62.
- Hall, M., Robin, C., Beate, B., Mothes, P., Monzier, M., 1999. Tungurahua Volcano, Ecuador: structure, eruptive history and hazards. *J. Volcanol. Geotherm. Res.* 91, 1–21.
- Hall, M., Mothes, P., Ramon, P., Arellano, S., Barba, D., Palacios, P., 2007. Dense Pyroclastic Flows of the 16–17 August 2006 Eruption of Tungurahua Volcano, Ecuador. AGU Joint Assembly, Acapulco, Mexico.
- Heiken, G., Wohletz, K., 1985. *Volcanic Ash*. University of California Press.
- Hill, B.E., Connor, C.B., Jarzempa, M.S., La Femina, P.C., Navarro, M., Strauch, W., 1998. 1995 eruptions of Cerro Negro volcano, Nicaragua, and risk assessment for future eruptions. *Geol. Soc. Am. Bull.* 110, 1231–1241.
- Houghton, B.F., Wilson, C.J.N., Del Carlo, P., Coltelli, M., Sable, J.E., Carey, R., 2004. The influence of conduit processes on changes in style of basaltic Plinian eruptions: Tarawera 1886 and Etna 122 BC. *J. Volcanol. Geotherm. Res.* 137, 1–14.
- Houghton, B.F., Swanson, D.A., Carey, R.J., Rausch, J., Sutton, A.J., 2011. Pigeonholing pyroclasts: insights from the 19 March 2008 explosive eruption of Kilauwa volcano. *Geology* 39, 263–266.
- Kelfoun, K., Samaniego, P., Palacios, P., Barba, D., 2009. Testing the suitability of frictional behaviour for pyroclastic flow simulation by comparison with a well-constrained eruption at Tungurahua volcano (Ecuador). *Bull. Volcanol.* 71, 1057–1075.
- Kumagai, H., Placios, P., Ruiz, M., Yepes, H., Kozono, T., 2011. Ascending seismic source during an explosive eruption at Tungurahua volcano, Ecuador. *Geophys. Res. Lett.* 38, L01306.
- Le Pennec, J.-L., Hall, M.L., Robin, C., Bartomioli, E., 2006. Tungurahua volcano—late Holocene activity. *Field Guide A1*. In: IAVCEI (Ed.), *Proceedings of the Fourth International Conference "Cities on Volcanoes"*, Quito, Ecuador.
- Le Pennec, J.-L., Jaya, D., Samaniego, P., Ramón, P., Moreno Yáñez, S., Egred, J., Van der Plicht, J., 2008. The AD 1300–1700 eruptive periods at Tungurahua volcano, Ecuador, revealed by historical narratives, stratigraphy and radiocarbon dating. *J. Volcanol. Geotherm. Res.* 176, 70–81.
- Le Pennec, J.-L., Ruiz, G.A., Ramon, P., Palacios, E., Mothes, P., Yepes, H., 2012. Impact of tephra falls on Andean communities: the influences of eruption size and weather conditions during the 1999–2001 activity of Tungurahua volcano, Ecuador. *J. Volcanol. Geotherm. Res.* 217–218, 91–103.
- McGimsey, R.G., Neal, C.A., Riley, C.M., 2001. Areal Distribution, Thickness, Mass, Volume, and Grain Size of Tephra-Fall Deposits from the 1992 Eruptions of Crater Peak Vent, Mt. Spurr volcano, Alaska. USGS Report 01-370.
- Miwa, T., Toramaru, A., Igushi, M., 2009. Correlations of volcanic ash texture with explosion earthquakes from vulcanian eruptions at Sakurajima volcano, Japan. *J. Volcanol. Geotherm. Res.* 184, 473–486.
- Molina, I., Kumagai, H., Le Pennec, J.-L., Hall, M., 2005. Three-dimensional P-wave velocity structure of Tungurahua Volcano, Ecuador. *J. Volcanol. Geotherm. Res.* 147, 144–156.
- Monzier, M., Robin, C., Samaniego, P., Hall, M.L., Cotton, J., Mothes, P., Arnaud, N., 1999. Sangay volcano, Ecuador: structural development, present activity and petrology 90, 49–79. *J. Volcanol. Geotherm. Res.* 90, 49–79.
- Nawotniak, S.E.K., Bursik, M., 2010. Subplinian fall deposits of Inyo Craters, CA. *J. Volcanol. Geotherm. Res.* 198, 433–446.
- Pioli, L., Erlund, E., Johnson, E., Cashman, K.V., Wallace, P., Rosi, M., Granados, H.D., 2008. Explosive dynamics of violent Strombolian eruptions: the eruption of Parícutin Volcano 1943–1952 (Mexico). *Earth Planet. Sci. Lett.* 271, 359–368.
- Pistolesi, M., Rosi, M., Cioni, R., Cashman, K.V., Rossotti, A., Aguilera, E., 2011. Physical volcanology of the post-twelfth-century activity at Cotopaxi volcano, Ecuador: behavior of an andesitic central volcano. *Geol. Soc. Am. Bull.* 123, 1193–1215.
- Pyle, D.M., 1989. The thickness, volume and grain-size of tephra fall deposits. *Bull. Volcanol.* 51, 1–15.
- Pyle, D.M., 2000. Sizes of volcanic eruptions. In: Sigurdsson, H. (Ed.), *Encyclopedia of Volcanoes*. Academic Press, pp. 263–269.
- Rose, W.I., 1993. Comment on 'another look at the calculation of fallout tephra volumes' by Judy Fierstein and Manuel Nathenson. *Bull. Volcanol.* 55, 372–374.
- Rose, W.I., Self, S., Murrow, P., Bonadonna, C., Durant, A.J., Ernst, G.G.J., 2008. Nature and significance of small volume fall deposits at composite volcanoes: Insights from the October 14, 1974 Fuego eruption, Guatemala. *Bull. Volcanol.* 70, 1043–1067.
- Rosi, M., Vezzoli, L., Castelmennano, A., Grieco, G., 1999. Plinian pumice fall deposit of the Campanian Ignimbrite eruption (Phlegrean Fields, Italy). *J. Volcanol. Geotherm. Res.* 91, 179–198.
- Rossotti, A., Carrasco-Núñez, G., Rosi, M., Di Muro, A., 2006. Eruptive dynamics of the "Citlaltépetl Pumice" at Citlaltépetl volcano, Eastern Mexico. *J. Volcanol. Geotherm. Res.* 158, 401–429.
- Samaniego, P., Le Pennec, J.-L., Robin, C., Hidalgo, S., 2011. Petrological analysis of the pre-eruptive magmatic process prior to the 2006 explosive eruptions at Tungurahua. *J. Volcanol. Geotherm. Res.* 199, 69–84.
- Sarna-Wojcicki, A.M., Shipley, S., Waitt Jr., R.B., Dzurisin, D., Woods, S.H., 1981. Areal distribution, thickness, mass, volume, and grain size of air-fall ash from the six major eruptions of 1980. In: Lipman, P.W., Mullineaux, D. (Eds.), *The 1980 Eruptions of Mount St. Helens, Washington*, vol. 1250. US Geol. Surv. Prof. Pap., pp. 577–600.
- Saucedo, R., Macias, J.L., Sheridan, M.F., Bursik, M.I., Komorowski, J.C., 2005. Modeling of pyroclastic flows of Colima Volcano, Mexico: implications for hazard assessment. *J. Volcanol. Geotherm. Res.* 139, 103–115.
- Savov, I.P., Luhr, J., Navarro-Ochoa, C., 2008. Petrology and geochemistry of lava and ash erupted from Volcán Colima, Mexico, during 1998–2005. *J. Volcanol. Geotherm. Res.* 174, 241–256.
- Scandone, R., Cashman, K.V., Malone, S.D., 2007. Magma supply, magma ascent and the style of volcanic eruptions. *Earth Planet. Sci. Lett.* 253, 513–529.
- Sheridan, M.F., Ragan, D.M., 1976. Compaction of ash-flow tuffs. In: Chilingarian, G.V., Wolf, K.H. (Eds.), *Compaction of Coarse-Grained Sediments. Developments in Sedimentology*, vol. 18B. Elsevier, Amsterdam, pp. 677–713.
- Sigurdsson, H., Carey, S., 1989. Plinian and co-ignimbrite tephra fall from the 1815 eruption of Tambora Volcano. *Bull. Volcanol.* 51, 243–270.
- Sparks, R.S.J., Bursik, M.I., Ablay, G.J., Thomas, R.M.E., Carey, S.N., 1992. Sedimentation of tephra by volcanic plumes. Part 2: controls on thickness and grain-size variations of tephra fall deposits. *Bull. Volcanol.* 54, 685–695.
- Sparks, R.S.J., Bursik, M.I., Carey, S.N., Gilbert, J.S., Glaze, L., Sigurdsson, H., Woods, A.W., 1997. *Volcanic Plumes*. John Wiley and Sons 577 pp.
- Steffke, A.M., Fee, D., Garces, M., Harris, A., 2010. Eruption chronologies, plume heights and eruption styles at Tungurahua Volcano: integrating remote sensing techniques and infrasound. *J. Volcanol. Geotherm. Res.* 193, 143–160.
- Streck, M.J., Dungan, M.A., Malavassi, E., Reagan, M.K., Bussy, F., 2002. The role of basalt replenishment in the generation of basaltic andesites of the ongoing activity at Arenal Volcano, Costa Rica; evidence from clinopyroxene and spinel. *Bull. Volcanol.* 64, 316–327.
- Sulpizio, R., 2005. Three empirical methods for the calculation of distal volume of tephra fall deposits. *J. Volcanol. Geotherm. Res.* 145, 315–336.
- Szramek, L., Gardner, J.E., Larsen, J., 2006. Degassing and microlite crystallization of basaltic andesite magma erupting at Arenal Volcano, Costa Rica. *J. Volcanol. Geotherm. Res.* 157, 182–201.
- Taddeucci, J., Pompilio, M., Scarlato, P., 2002. Monitoring the explosive activity of the July–August 2001 eruption of Mt. Etna (Italy) by ash characterization. *Geophys. Res. Lett.* 29, 1230.
- Taddeucci, J., Pompilio, M., Scarlato, P., 2004. Conduit processes during the July–August 2001 explosive activity of Mt. Etna (Italy): inferences from glass chemistry and crystal size distribution of ash particles. *J. Volcanol. Geotherm. Res.* 137, 33–54.

- Valade, S., Donnadieu, F., 2011. Ballistics and ash plumes discriminated by Doppler radar. *Geophys. Res. Lett.* 38, L22301.
- Varley, N., Arambula-Mendoza, R., Reyes-Davila, G., Sanderson, R., Stevenson, J., 2010. Generation of Vulcanian activity and long-period seismicity at Volcán de Colima, Mexico. *J. Volcanol. Geotherm. Res.* 198, 45–56.
- Walker, G.P.L., Croasdale, R., 1971. Two plinian-type eruptions in the Azores. *J. Geol. Soc. London Mem.* 127, 17–55.
- Walker, G.P.L., Wilson, L., Bowell, E.L.G., 1971. Explosive volcanic eruptions-I the rate of fall of pyroclasts. *Geophys. J. R. Astron. Soc.* 22, 377–383.
- Walker, G.P.L., 1973. Explosive volcanic eruptions—a new classification scheme. *Geol. Rundsch.* 62, 431–446.
- Walker, G.P.L., 1980. The Taupo pumice: product of the most powerful known (ultraplinian) eruption? *J. Volcanol. Geotherm. Res.* 8, 69–94.
- Wright, H.M.N., Cashman, K.V., Mothes, P.A., Hall, M.L., Ruiz, A.G., Le Pennec, J.L., 2012. Estimating rates of decompression from textures of erupted ash particles produced by 1999–2006 eruptions of Tungurahua volcano, Ecuador. *Geology* 40, 619–622.
- Yamanoi, Y., Takeuchi, S., Okumura, S., Nakashima, S., Yokoyama, T., 2008. Color measurements of volcanic ash deposits from three different styles of summit activity at Sakurajima volcano, Japan: conduit processes recorded in color of volcanic ash. *J. Volcanol. Geotherm. Res.* 178, 81–93.